Progress In Electromagnetics Research C, Vol. 128, 129–142, 2023

Design and Validation of Reflector Elements to Increase the Radar Cross-Section of Small Drones

Alex Ganau*, Joaquin Vico, Pablo Morcillo, and Juan V. Balbastre

Abstract—In the next few years, the use of drones for civilian applications is expected to skyrocket, leading to a multitude of new use cases. However, the possible improper use of drones generates doubts due to the risks it poses to the safety and security of airspace operations. Having absolute surveillance of unmanned aircraft is quite difficult for several reasons, e.g., problems arise when monitoring small drones due to their reduced radar signature, around $-10\,\mathrm{dBm}^2$, which makes them practically imperceptible to Air Traffic Control (ATC) radars, which can rarely detect targets with Radar Cross-Sections (RCSs) below $0\,\mathrm{dBm}^2$. A possible solution to mitigate the lack of identification and thus avoid problems specially in Control Traffic Region (CTR) zones is to increase the RCSs of the drones by incorporating a reflector element that could produce much more intense radar echoes than the drone itself. The aim of this paper is to design a Luneburg lens through electromagnetic (EM) simulation and validate its performance experimentally running flight tests making use of a 24 GHz radar and a commercial drone.

1. INTRODUCTION

Safety and security are unquestionably key aspects in aviation industry. Since people's trust largely contributes to the growth in this sector, it is crucial to improve air traffic by deploying newer, safer, and more secure systems; hence, appropriate measures should be taken when designing more advanced aerial vehicles. Continuous Unmanned Aerial Systems (UASs) development and investment has really shot up to an extent that drones market shifted from being unnoticed to becoming a world economic power given its smashing impact on lots of sectors and daily applications [1]. As a matter of fact, leisure activities stand out among the leading purposes for the use of drones in the next few years, followed by government and commercial sectors, mainly focusing on public safety and security issues, among others.

Although it may seem that deploying hundreds of drones runs smoothly at a glance, having absolute control over the air traffic of unmanned craft is very difficult for many different reasons. According to the Commission Delegated Regulation (EU) 2019/945 [2], when failures in drones' electronic identification (eID) appear, while heavy and large Remotely Piloted Aircraft Systems (RPASs) have significant RCS so as to be detected by aeronautical radars, in the case of light RPAS, whose weight does not usually exceed 25 kg, problems arise when their presence is monitored due to their small physical radar signature, around $-10\,\mathrm{dBm}^2$, and their relatively low speed, around 20 m/s, which make them practically imperceptible to ATC radars, due to the Sensitivity Velocity Control (SVC) used to suppress echoes from small and slow targets such as birds. Addressing this problem will have practical benefits for the future of the aviation sector, since the number of Unmanned Aerial Vehicles (UAVs), or drones, that will be included in non-segregated airspace along with conventional airliners will rise considerably in the near future.

This paper aims to design and validate a reflector element to increase the RCS of small drones when they are observed by a ground-based radar placed in front of the aircraft. EM simulation tools

Received 20 September 2022, Accepted 7 December 2022, Scheduled 4 January 2023
* Corresponding author: Alex Ganau (algasan6@teleco.upv.es).
The authors are with the Universitat Politècnica de València, Valencia, Spain.

will be used to study several alternatives in order to build a low-cost, low-weight aerodynamic object so as not to affect flight autonomy nor drones airworthiness, and thus, attending the existing need of having a back-up method of monitoring drones from the ground in case of eID failure, specially in high risk operations such as those in vertiports or drone landing pads, therefore, guaranteeing everybody's safety. When looking for an easy, fast, and low-cost manufacturing process, 3D printing is the most feasible solution. Subsequently, measures will be taken to test the reflector by means of a 24 GHz radar in an anechoic chamber before running flight tests with a commercial drone. Regardless of the drone, the reflector would be placed on the bottom side of the airframe with the RCS maximum on the head-on direction.

This paper is divided into seven sections, which will address the Luneburg lens properties and applications, the model design and simulation results, the 3D printing techniques which will include two different approaches of the reflector design and manufacturing, the material and methods describing the sites, software and drone used, the laboratory measurements to study the performance of the lenses, the flight tests, and finally, the conclusions summing up key aspects accomplished during this research.

2. LUNEBURG LENS

A standard Luneburg lens [3] consists of a spherically symmetric multi-refractive device with a graded permittivity profile that varies radially from the center to the outer surface of the lens (Equation (1)),

$$\epsilon_r(r) = 2 - \left(\frac{r}{R}\right)^2 \tag{1}$$

where R is the radius of the lens. Although commonly associated with parabolic dishes, these lenses are not confined to a single optical axis because their symmetric property. Typically, the lens is partially coated with a metallic reflective layer that enables it to focus EM waves entering the lens from the open hemisphere on incident angle-dependent focal points and reflect the energy directly back to the source in the same direction. No reflection occurs at the surface since its refractive index is the same as that of the surrounding medium. Figure 1 shows the paths of the rays within a Luneburg lens along with its corresponding cross-section, with blue shading proportional to its refractive index.

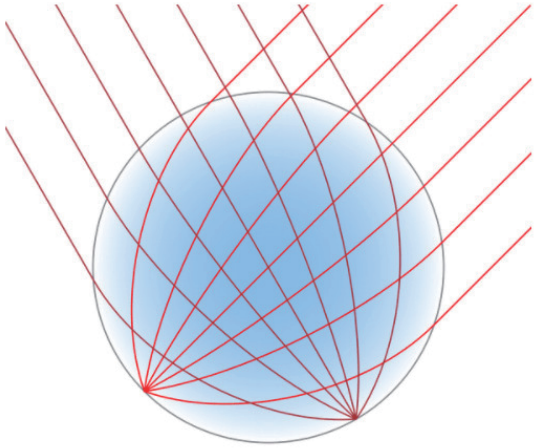

Figure 1. Cross-section of a standard Luneburg lens, with blue shading proportional to the refractive index. Photo extracted from Wikipedia, 2009.

Luneburg lenses have lots of civilian applications. However, its major use occurs in the military field. Its small size and prominent directional pattern make this lens a unique radar reflector to let the RCS area reflected by the lens be up to tens or hundreds times larger than the objects' physical RCS.

For this reason, fighter jets like F-35, which have every angle and surface precisely machined to baffle radar waves, incorporate several Luneburg lenses in their structures (see Figure 2) while flying over

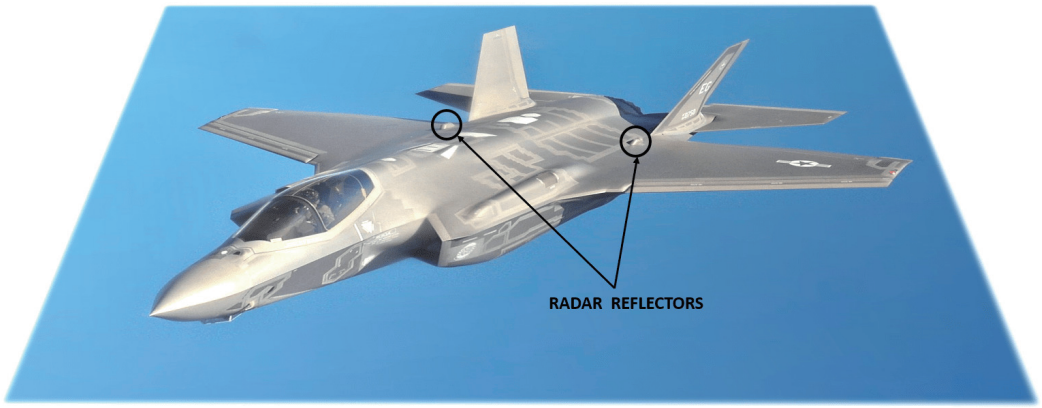

Figure 2. Lockheed Martin F-35 Lightning II incorporating Luneburg lenses as radar reflectors. Photo taken by Master Sgt. Donald R. Allen, Eglin U.S. Air Force Base, FL, US, 2013.

friendly airspace outside wartime in order to avoid potential crashes between non-detected fighters and their allies planes. Thanks to these lenses, monitoring the so-called invisible jets that would normally be nearly impossible for civilian ATC to spot has prevented the loss of billions of dollars in war systems so far. Deploying removable lenses, and thus, by manipulating the RCS in stealth fighters not only conceals their radar signature, but also prevents anti-stealth experiments by the adversaries during wartime.

3. MODEL DESIGN

Figure 3 shows the scenario considered to develop the Luneburg lens presented in this paper, in line with the EASA prototype specification for vertiports [4]. The idea is to create a reflector that could allow the ground radar to be aware of the existence of drones in the approach and take-off climb areas.

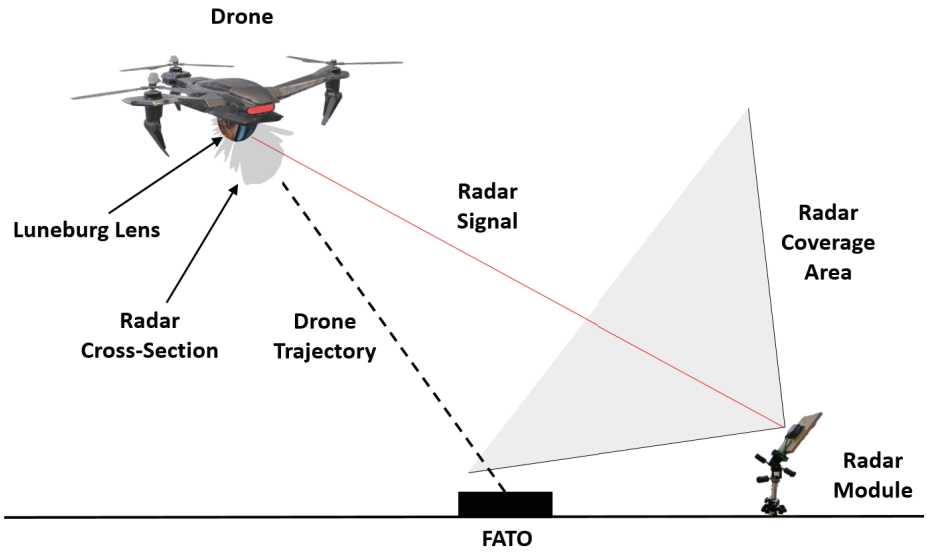

Figure 3. representation of a likely scenario.

To this purpose, a hemispherical Luneburg lens reflector was proposed in view of reducing height and weight as much as possible to avoid potential airworthiness problems. This model, designed in the EM software FEKO®, was built on a 9 cm-diameter outer sphere. With the aim of reducing the impact

Table 1. Radii and relative permittivities of the Luneburg lens.

	R_o (mm)	R_i (mm)	R_c (mm)	ϵ_r
Hemisphere 1	45	35	40	1.2098
Hemisphere 2	35	25	30	1.5556
Hemisphere 3	25	15	20	1.8024
Hemisphere 4	15	5	10	1.9506
Hemisphere 5	5	0	2.5	1.9969

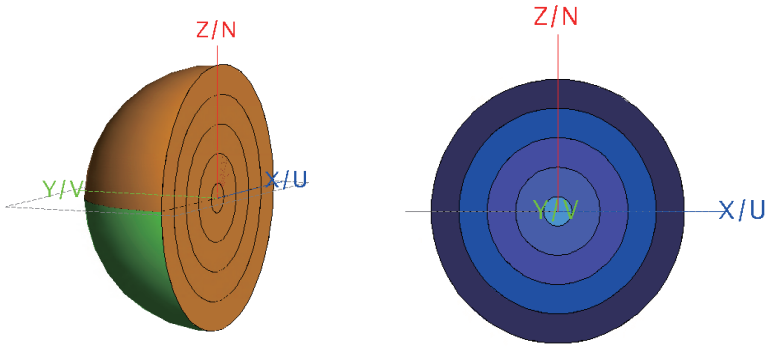

(a) (b)

Figure 4. Proposed Luneburg lens coated with PEC. (a) Geometry of the lens where colors orange and green stand for the PEC covered and uncovered parts of the surface, respectively and (b) set-up of the five dielectric layers (rear view) with different shades of blue representing each of the five regions used.

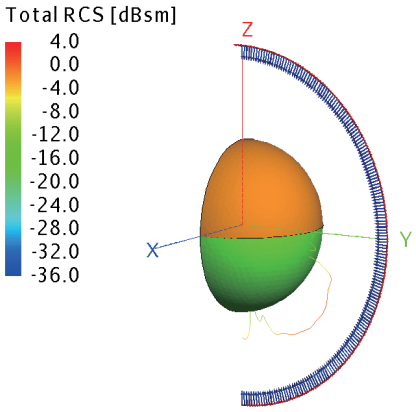

Figure 5. Monostatic RCS of the Luneburg lens (logarithmic scale).

on the drone's aerodynamic profile and considering that only the reflections towards the ground are relevant (as shown in Figure 3), only half of the spherical lens was used, coating the base and half of the external surface of the resulting hemisphere with a Perfect Electric Conductor (PEC) layer. The proposed lens consists of a series of five spherical layers (see Figure 4(b)) with constant permittivity that approximates the permittivity profile of the lens given by Equation (1) to a stepped function. In addition, the geometry and dielectric properties of this Luneburg lens are listed in Table 1, where R_o, R_i, R_c represent the outer, inner, and center radii of the regions, and ϵ_r is the corresponding dielectric constant.

Figure 5 shows the monostatic RCS in logarithmic scale of the Luneburg lens described on Figure 4

at 24 GHz (considering that the radar relative bandwidth is less than 1%, and the design was only conducted at the carrier frequency). Moreover, the blue semicircle represents the 180 directions of incidence of the linearly polarized (parallel to the z axis) plane waves used to get the scattered fields from which the RCS is computed, simulating the possible radar incident waves, according to the layout shown in Figure 3. In addition, Figure 6 depicts the RCS on the $x = 0$ plane for $y > 0$ (referred to the axes in Figure 5).

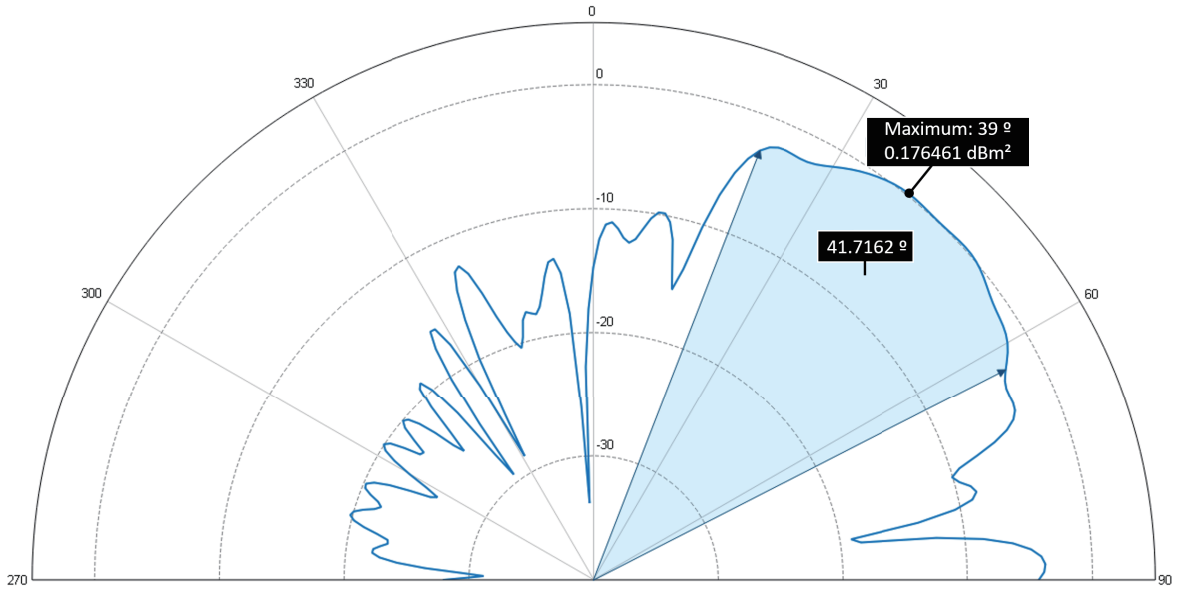

Figure 6. Far field of the Luneburg lens.

Two important characteristic parameters of this Luneburg lens can be extracted from Figure 6.

- *Half power beamwidth (−3 dB)*: $\Delta\theta_{-3\,dB} = 41.7162°$.
- *Global maximum*: $0.176461\,\mathrm{dBm}^2$ ($1.0414\,\mathrm{m}^2$), at 39°.

Ideally, the RCS should be constant between 0° and 90°. However, this is physically impossible due to the finite dimensions of the metallic surfaces. This lens provides a great *Half power beamwidth (−3 dB)* with a consistent global maximum ($\sigma \simeq 1\,\mathrm{m}^2$). This value is similar to the RCS of an adult human or a small single-engine aircraft, despite the lens' small size, very promising results for this application.

4. 3D PRINTING

Once the simulated model has been developed and validated, a prototype for experimental testing was created. This prototype was constructed with 3D manufacturing processes in mind to benefit from the quick turn-over times and low cost of 3D printing. For the purposes of this paper, two different materials were considered for this construction, Acrylonitrile Butadiene Styrene (ABS) filament and UV resin.

4.1. Fused Deposition Modeling

The lens was printed with a *Zortrax M200 Plus* using a Fused Deposition Modeling technology, a method in which melted material (ABS) is deposited layer by layer onto the built platform to create the desired object. It is characterized by using a 90–390 microns layer resolution and a minimal wall thickness of 450 microns. In order to achieve the different permittivities listed in Table 1, the variation of ϵ was first characterized. To this purpose, three different samples or Devices Under Test (DUTs) (cylinders of

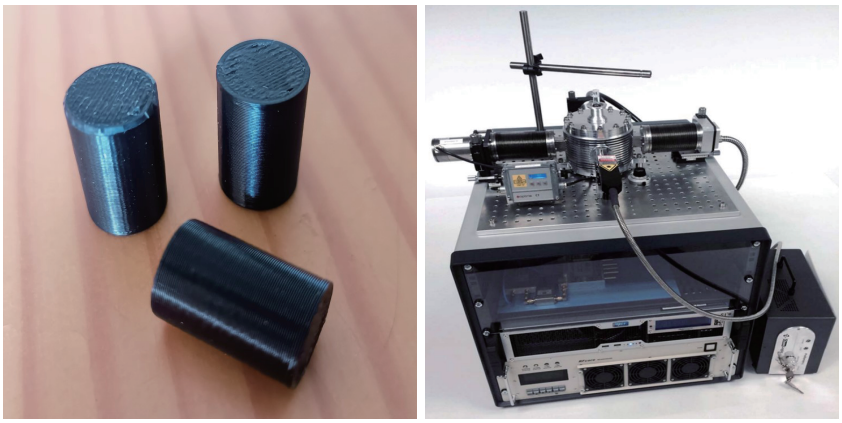

(a) (b)

Figure 7. (a) Samples and (b) dual mode microwave cavity.

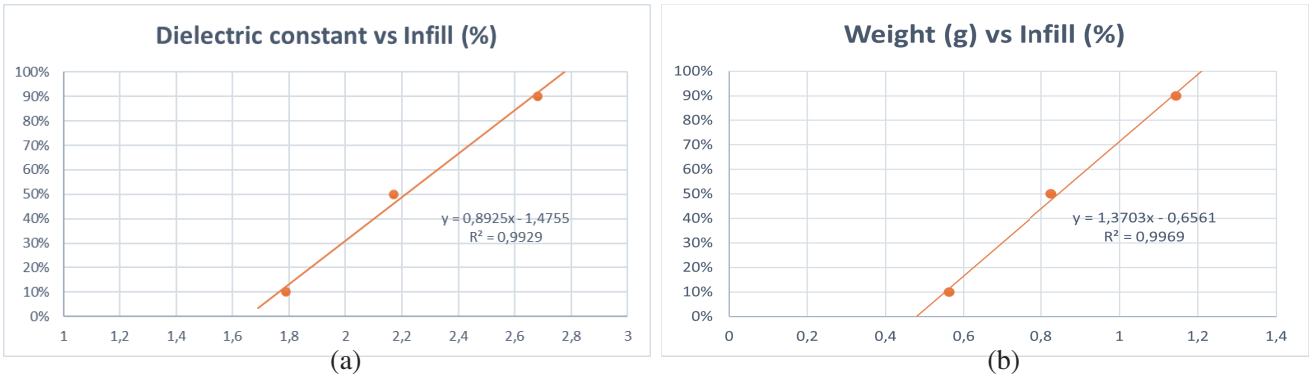

(a) (b)

Figure 8. Graphs of the infill percentage. (a) Dielectric vs infill and (b) weight vs infill.

Table 2. Permittivities of the samples for different infill values.

Infill (%)	10	50	90
Weight (g)	0.562	0.825	1.144
Relative density (%)	46.4	68.2	94.5
ϵ'	1.79	2.17	2.68
ϵ''	0.009	0.0134	0.0166

diameter 9.8 mm and height 15 mm, shown in Figure 7(a)) were printed, and their permittivity values were measured using the method described in [5] with a dual mode microwave cavity (see Figure 7(b)).

Table 2 shows the measured permittivities and weights for each sample whereas Figure 8 depicts two graphs that represent the permittivities and weights with regard to the corresponding infill values, attaining very good linear regressions, with $R^2 = 0.9929$ and $R^2 = 0.9969$, respectively. The target weights of the hemispheres listed in Table 3 were calculated through a series of interpolations from Figure 8(b). Afterwards, each hemispherical layer was assigned several infill percentages, giving rise to the attainment of different weights (see Table 4). Hence, approaching as much as possible *Target weight* from Table 3 was necessary to select the optimal infill percentage for the subsequent printing process.

As can be observed in Table 4, several *Infill-Weight-Ratio* analyses were realized, where *Ratio* (%) is the result of the division between a certain *Weight* from Table 4 and *Weight if bulk PVC* from Table 3.

Table 3. Infill over bulk and target weight of the five regions.

	ϵ_r	Infill over bulk (%)	Weight if bulk PVC (g)	Target weight (g)
Hemisphere 5	1.9969	73.1	0.3168	**0.232**
Hemisphere 4	1.9506	71.5	8.218	**5.872**
Hemisphere 3	1.8024	66.0	30.876	**20.385**
Hemisphere 2	1.5556	57.0	68.59	**39.08**
Hemisphere 1	1.2098	44.3	121.359	**53.78**

Table 4. Print-weight-ratio values of the spheres characterization.

	Infill (%)	Weight (g)	Ratio	Infill (%)	Weight (g)	Ratio	Infill (%)	Weight (g)	Ratio
Hemisphere 5	30	0.1897	59.9	50	0.1919	60.6	80	**0.2453**	77.4
Hemisphere 4	80	4.917	59.8	90	5.58	67.9	90	**5.603**	68.2
Hemisphere 3	60	16.98	55.0	80	18.382	59.5	90	**20.739**	67.2
Hemisphere 2	80	**40.35**	58.8						
Hemisphere 1	60	**54.85**	45.2						

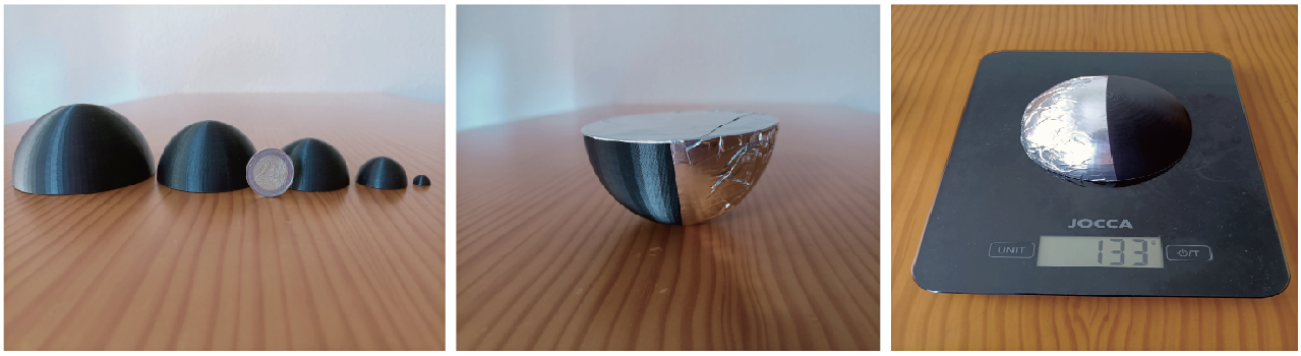

(a) (b) (c)

Figure 9. Filament lens. (a) Dielectric regions, (b) final appearance of the lens and (c) final weight.

Bold font in Table 4 represents the final weight values achieved after some approximations.

Figure 9 shows the hemispheres of the Luneburg lens along with the final appearance and its weight.

4.2. Stereolithography Apparatus

Another alternative was to fabricate the lens with a different construction technology, in this case, by Stereolithography Apparatus (SLA), commonly known as resin 3D printing. This type of machines are all built around the same principle, using a light source, either a laser or projector, to cure liquid resin into hardened plastic that gives shape to the object layer by layer. For this approach, a new filling configuration is needed to be proposed so as to achieve the required permittivity all along the different regions of the lens by using a dielectric material with permittivity $\epsilon_1 = 2.92$. Equation (2) represents the expression to obtain the proposed filling ratio for different permittivities. Variable C depends on the *Cells* used for every dielectric region and can be selected as desired, provided that the subsequent filling requirements are feasible, and section $a \cdot b$ is determined by a rectangle of dimensions 15 mm $\times$ 7.5 mm.

$$\epsilon_r = \frac{C \cdot c \cdot d \cdot \epsilon_0 + (a \cdot b - C \cdot c \cdot d) \cdot \epsilon_1}{a \cdot b} \tag{2}$$

Table 5. Free-space sections for the proposed filling configuration.

	ϵ_r	c · d · C
Hemisphere 5	1.9969	2.22
Hemisphere 4	1.9506	3.11
Hemisphere 3	1.8024	3.59
Hemisphere 2	1.5556	8.76
Hemisphere 1	1.2098	10.98

Table 5 gathers the $c \cdot d \cdot C$ free-space sections, in mm^2, depending on the permittivities of the five hemispheres. To design this resin model, *Autodesk Inventor* ® was used for the filling configuration.

Figure 10 shows the filling layout whereas Figure 11 depicts the final lens along with its weight. Section $a \cdot b$ from Figure 10(a) can also be appreciated in the lower inner part of Figure 10(b) along with its expansion for the entire dielectric region range, repeating the previously established configuration.

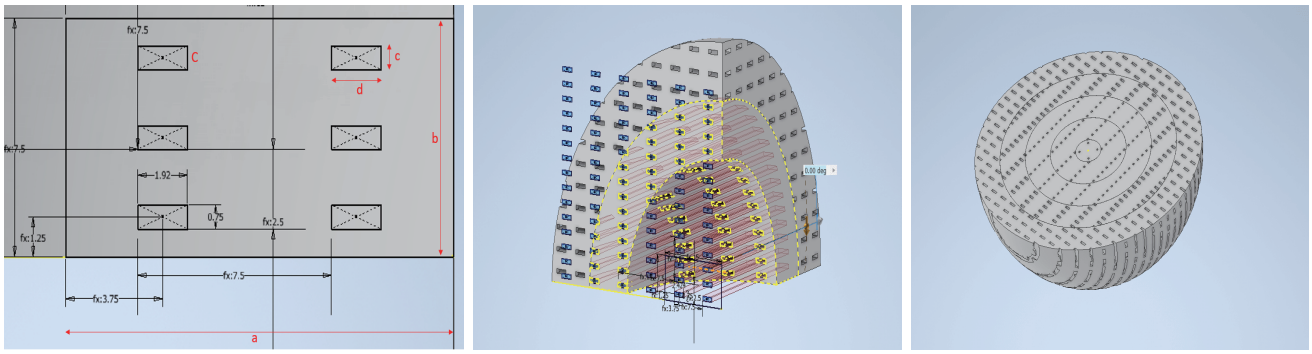

(a) (b) (c)

Figure 10. Proposed filling layout. (a) 2D-View dimensions, (b) 3D-View dimensions and (c) perspective view of the filling configuration applied on the complete Luneburg lens.

(a) (b) (c)

Figure 11. Resin lens. (a) Dielectric regions, (b) final appearance of the lens and (c) final weight.

5. MATERIAL AND METHODS

This section includes a description of the different indoor and outdoor locations needed to run the measurements, the radar software used for simulations, and the drone utilized for the final flight tests.

5.1. Anechoic chamber

Initially, considering the performance study of the manufactured lenses, in terms of EM isolation, radar measurements took place in a 3 m × 4 m anechoic chamber (see Figure 12) to suppress all possible interferences so that appropriate results could be obtained. The objective was to assess and understand the behavior of the dielectric reflectors. For that reason, the lenses were placed on top of a piece of absorbent material so that when simulating electromagnetically, it would not interfere with the results, giving rise to unwanted echoes or other problems that might eventually arise. The radar was positioned on the front wall at mid-height and at a distance of 4 m with respect to the targets (lenses). An adjacent room was used by the staff in charge of running simulations to avoid interferences from showing up.

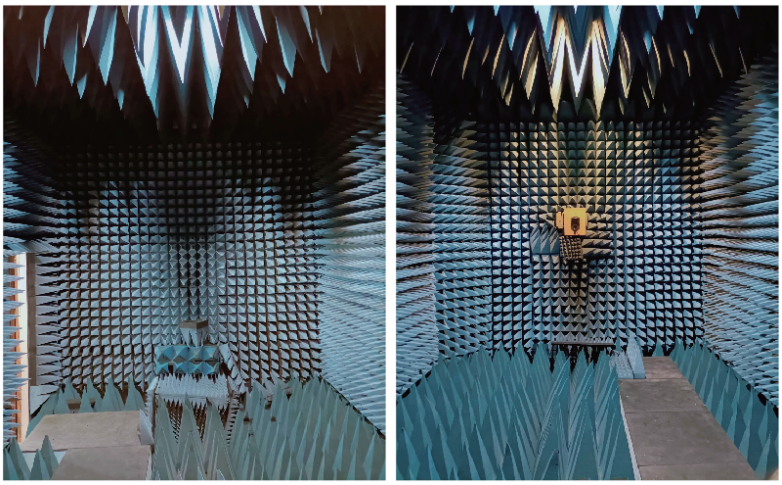

(a) (b)

Figure 12. Anechoic chamber. (a) Lens position and (b) radar placement.

5.2. IMST Radar Module

For simulations, the *IMST DK-sR-1200 Radar Module* [6] was used (see Figure 13). For the application described in this paper, the radar operates in Frequency-Modulated Continuous Wave (FMCW) mode at a carrier frequency of 24 GHz with a frequency range of 230 MHz (bandwidth), with minimum frequency starting on 24008 MHz. The FMCW performance is determined by the Effective Isotropic Radiated Power (EIRP), also known as output power, which is tunable between 10 dBm and 19 dBm. When the *IMST SenTool* software is launched, a few operating modes appear available to the user depending on

(a) (b)

Figure 13. DK-sR-1200 Radar Module. (a) Case and (b) hardware.

the necessity of the application. Hereby, two types of plots stand out. The *Polar Plot* was used to test the performance of the lenses inside the anechoic chamber statically, whereas the *Human Tracker Plot*, based on the Human Tracker Algorithm, was used for flight tests, given the possibility to detect and track moving targets over a static background scene, typically used for many security applications.

5.3. Fly Test Site

Flight tests were run in an airfield in the northwest of the city of Valencia (Spain), out of the airport Controlled Traffic Region (CTR) where drone flights in the open category can be conducted without the need of any permissions. It consists of a 235 m × 40 m area aimed at enabling unmanned aerial flights and other telecommunications-related studies when wide open space is needed (see Figure 15(a)).

5.4. Drone

The commercial drone used for the subsequent flight tests was the DJI Flame Wheel 450 (F450), characterized by a *Diagonal Wheelbase* of 450 mm and a *Takeoff Weight* up to 1,600 g (see Figure 16(a)).

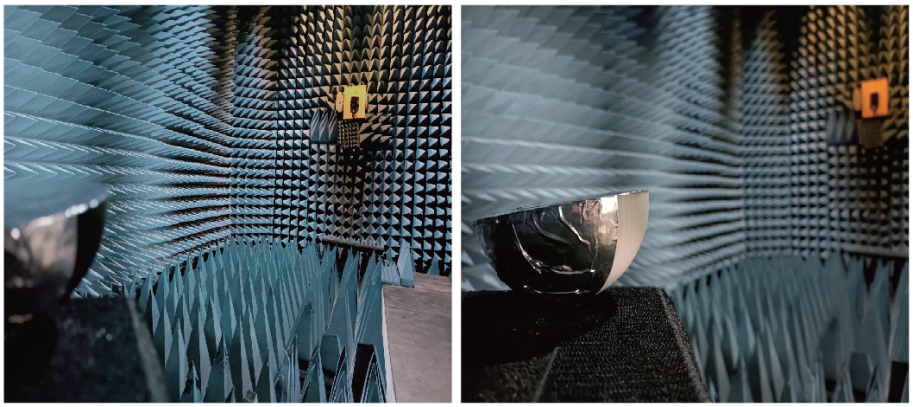

(a) (b)

Figure 14. Luneburg lenses during Polar Plot tests. (a) Filament lens and (b) resin lens.

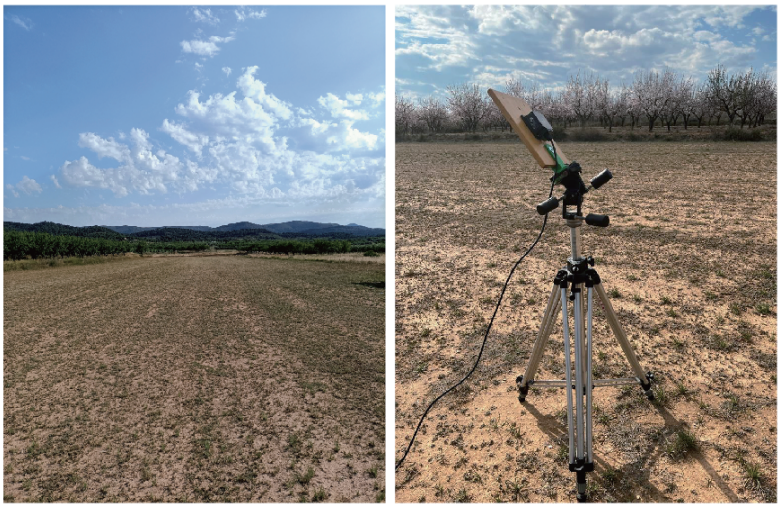

(a) (b)

Figure 15. (a) Airfield and (b) radar module on the tripod.

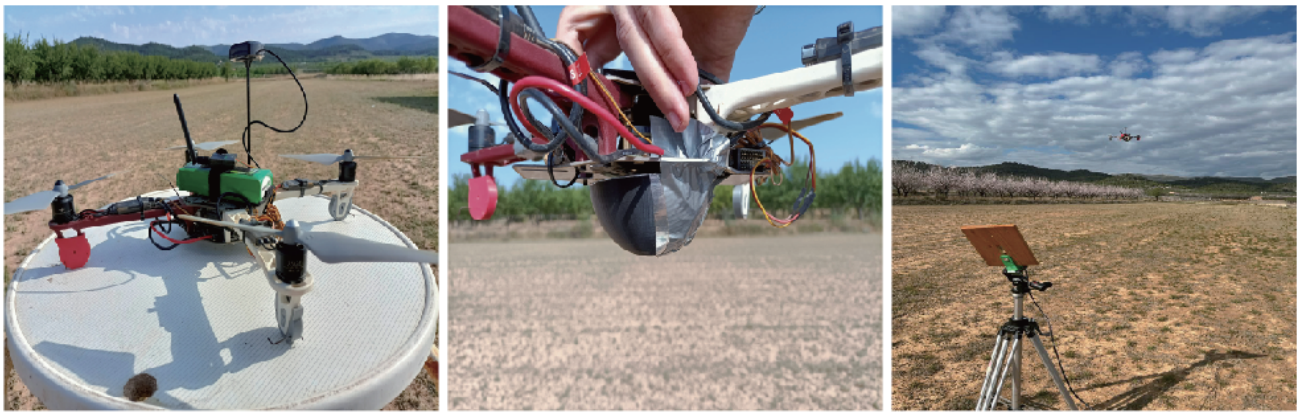

(a) (b) (c)

Figure 16. (a) Drone used, (b) drone with the lens and (c) drone during a flight test.

6. LABORATORY MEASUREMENTS

6.1. RCS of a Metallic Sphere

Initially, a 20 cm-diameter chrome silver metallized cork sphere was used for starting measurements. Contrary to the *Human Tracker Plot*, the *Polar Plot* does not compute nor show the received power of targets, so an alternative solution was thought to be appropriate based on an approximation which entails the RCS of the target and a threshold value for detection. On the basis of the RCS emitted from a sphere of diameter D, it can be obtained as the geometric area of the sphere following Equation (3),

$$\sigma_{sphere} = A_{geom} = \pi \left(\frac{D}{2}\right)^2 \tag{3}$$

where D is the diameter. Since $D = 20\,\text{cm}$, the RCS is $\sigma_{sphere} = -15\,\text{dBm}^2$. An approximate threshold of $-16\,\text{dBm}$ was found on the software as the limit to allow the correct sphere's detection.

6.2. RCS of the Filament Lens

Secondly, a filament lens was analyzed, obtaining a threshold value of $-3\,\text{dBm}$. An approximation (Equation (4)) was used to relate this limiting value with the corresponding RCS of this Luneburg lens,

$$\sigma_{lens} \simeq \sigma_{sphere} \cdot \frac{P_{lens}}{P_{sphere}} \simeq \sigma_{sphere} \cdot \frac{Th_{lens}}{Th_{sphere}} \tag{4}$$

where σ_{lens} and σ_{sphere}, P_{lens} and P_{sphere}, Th_{lens} and Th_{sphere} are the RCS, the received power and threshold values of both the lens and the metallic sphere, respectively. Since $\sigma_{sphere} = -15\,\text{dBm}^2$, $Th_{sphere} = -16\,\text{dBm}$, and $Th_{lens} = -3\,\text{dBm}$, the respective RCS of this filament lens is $\sigma_{lens} = -2\,\text{dBm}^2$.

6.3. RCS of the Resin Lens

Last but not least, tests were conducted to the resin lens so as to select the reflector providing a better performance. This time, the threshold value found was $-8\,\text{dBm}$. Following Equation (4), since $\sigma_{sphere} = -15\,\text{dBm}^2$, $Th_{sphere} = -16\,\text{dBm}$ and $Th_{lens} = -8\,\text{dBm}$, the RCS of this resin lens is $\sigma_{lens} = -7\,\text{dBm}^2$. In addition, Figure 14 shows both lenses during *Polar Plot* simulations inside the anechoic chamber.

7. FLIGHT TESTS

Considering the results of the measurements performed in the anechoic chamber, it was decided to use the filament lens for the flight tests, not the resin lens, due to its lighter weight and better RCS. Besides, the rest of the section describes the experimental setup and the results obtained with this reflector.

7.1. Flight Test Description

The flight setup was configured to reproduce the scenario shown in Figure 3. For this reason, the radar was placed on the top of a tripod (Figure 15(b)) and tilted 40° to prevent ground reflections from affecting measurements. The drone trajectory (Figure 17) was defined assuming that the approach lane had a slope of 40°, i.e., aligned with the radar tilt (this is a value representative of actual drone operations).

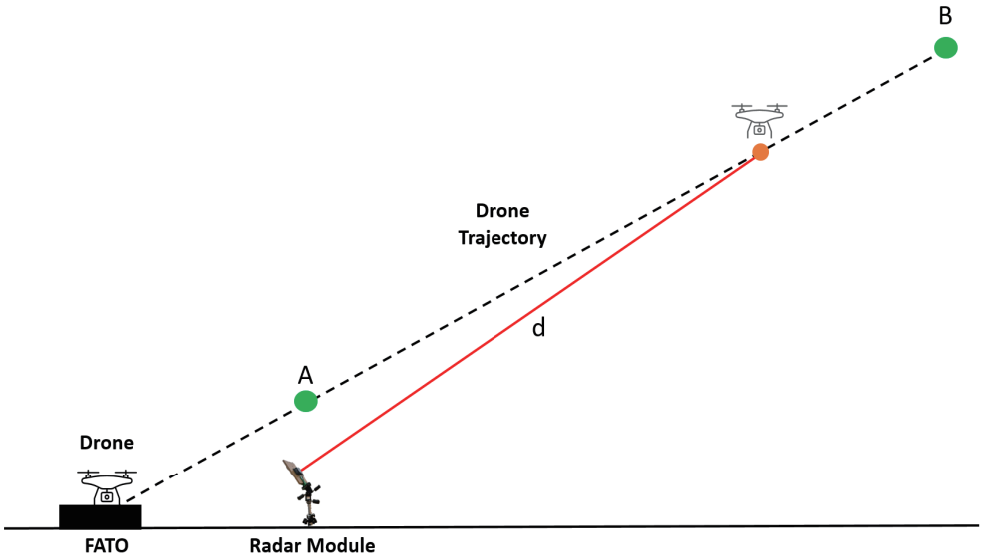

Figure 17. Representation of the drone trajectory.

The *Human Tracker Plot* mode from the radar module [6] was used for flight measurements. As mentioned before, this method can be applied to detect and track moving targets over a static background scene. The first measurements were taken to the drone alone and then to the drone fitted with the lens (see Figure 16 for details), to assess whether it improved the drone's detectability or not.

Figure 17 is aimed at representing the actual scenario configured for measurements, indicating the drone trajectory. As can be observed in the figure, the vertiport's Final Approach and Take-Off area (FATO) is located behind the radar module, and the drone enters the radar coverage volume at point A (4 m of altitude), with a clearance distance of 2 m above the radar. After a set of preliminary measurements, the final point of the trajectory was set at point B (55 m of altitude) to ensure that the drone would be detected by the radar in all the tests. Distance d represents the detection distance.

7.2. Flight test results

Figure 18 illustrates a Box and Whisker plot with the maximum drone's trackable distances before and after using the dielectric reflector, for five different flight tests. It is very easy to see that when the Luneburg lens was added, the maximum detection distances more than doubled those without the reflector.

Measurements might differ depending on the weather conditions, drones characteristics, placement of the dielectric reflector, and some other relevant factors. A parallel checking could be done through

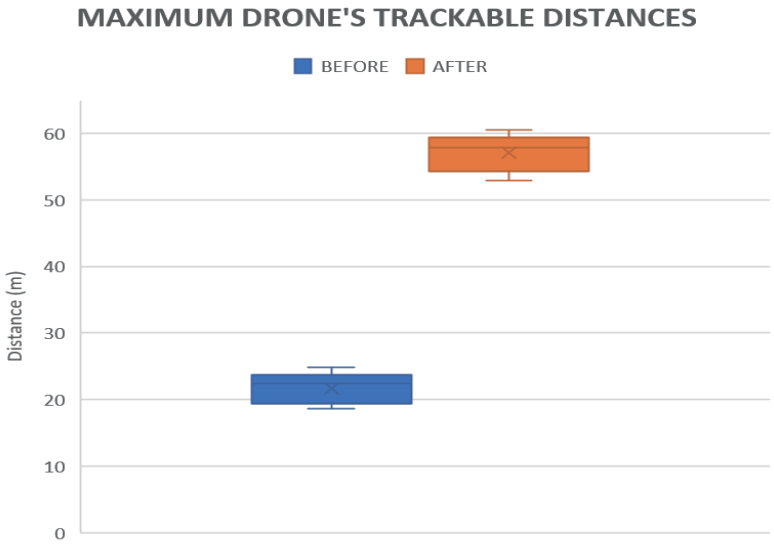

Figure 18. Maximum drone's trackable distances.

a Python example code provided by the radar manufacturer, which was modified by the co-authors of this paper for this application. It is accessible in https://github.com/algasan6/PythonScript.

Considering the results from the flight tests run before and after adding the lens (Figure 18), the statistical parameters are listed in Tables 6 and 7, respectively, clearly demonstrating the improvements.

Table 6. Before adding the Luneburg lens.

Lower quartile	Q_1	19.35 m
Upper quartile	Q_3	23.70 m
Median	Q_2	22.50 m
Minimum	Min	18.60 m
Maximum	Max	24.80 m

Table 7. After adding the Luneburg lens.

Lower quartile	Q_1	54.25 m
Upper quartile	Q_3	59.40 m
Median	Q_2	57.80 m
Minimum	Min	52.90 m
Maximum	Max	60.50 m

8. CONCLUSIONS

In this paper, the design and consequent EM study of a dielectric reflector has been presented, from the initial design to the final validation through flight tests. The designed reflector, a so-called Luneburg lens, provides great *Half power beamwidth* (-3 dB) and a consistent maximum back-scattering RCS. The RCS behavior produced by this lens resulted in a very promising response for this type of application. As for the construction process, this Luneburg lens was fabricated by means of two different 3D printing techniques, FDM and SLA. Indoor measurements were taken to analyze electromagnetically both

manufactured lenses and test its validity and performance. The RCS measurements in an anechoic chamber clearly demonstrated the superiority of one of the two lenses in terms of RCS, which is also the lighter lens, so the filament lens was chosen to be used in open-air flight tests. Regarding the insertion of the reflector on the drone, the lens did not impact the drone's stability nor affect its airworthiness at any time during the tests due to its small size, lightness, and aerodynamic profile. The results of the experimental validation, shown in Figure 18 and Tables 6 and 7, clearly demonstrate the great success and benefits of using the designed reflector, increasing the maximum detection distances considerably thanks to the enhancement of the RCS. In this way, drones become passively conspicuous for radars without the need of any active device, thus enabling higher levels of safety in drone operations.

ACKNOWLEDGMENT

The authors thank Mr Pedro Plaza González, from the UPV ITACA DIMAS group and Mr Alberto Santonja Gimeno, from the UPV ETSID for their support in manufacturing the prototypes of the lenses.

REFERENCES

1. SESAR Joint Undertaking, *European Drones Outlook Study*, Publications Office of the European Union, Nov. 2016.
2. EASA, "Commission Delegated Regulation on unmanned aircraft systems and on third-country operators of unmanned aircraft systems," *Commission Delegated Regulation (EU)*, 2019/945, Mar. 2019.
3. Luneburg, R. K., *Mathematical Theory of Optics*, University of California Press, Berkeley and Los Angeles, 1964.
4. EASA, *Prototype Technical Design Specifications for Vertiports*, Mar. 2022.
5. Catalá-Civera, J. M., A. J. Canós, P. Plaza-González, J. D. Gutiérrez, B. García-Baños, and F. L. Peñaranda-Foix, "Dynamic measurement of dielectric properties of materials at high temperature during microwave heating in a dual mode cylindrical cavity," *IEEE Transactions on Microwave Theory and Techniques*, Vol. 63, No. 9, 2905–2914, Sept. 2015, doi: 10.1109/TMTT.2015.2453263.
6. IMST GmbH, *IMST sentireTM Radar Module DK-sR-1200 Development Kit User Manual*, Carl-Friedrich-Gauss Str. 2-4, 47475 Kamp-Lintfort, Germany, Version 1.11, 2018.